Eur. Phys. J. Plus (2025) 140:367
https://doi.org/10.1140/epjp/s13360-025-06305-0

THE EUROPEAN PHYSICAL JOURNAL PLUS

Regular Article

Modular apparatus for nuclear reactions spectroscopy (MARS): characterization and first application to determine $^{12}C(^{6}Li,^{4}He)^{14}N^{g.s}$ nuclear reaction cross sections

L. Garrido-Gómez[1,a], **A. Vegas-Díaz**[1,2], **M. A. G. Alvarez**[1], **J. P. Fernández-García**[1], **B. Fernández**[1,2], **F. J. Ferrer**[1,2], **D. Lopez-Aires**[3]

[1] Departamento FAMN, Universidad de Sevilla, Apartado 1065, 41080 Sevilla, Spain
[2] Centro Nacional de Aceleradores, Universidad de Sevilla, Junta de Andalucía-CSIC, 41092 Sevilla, Spain
[3] Institute for Transuranium Elements ITU, European Commission - Joint Research Centre, Box 2340, 76125 Karlsruhe, Germany

Received: 23 February 2025 / Accepted: 6 April 2025

Abstract This work presents MARS (Modular apparatus for nuclear reactions spectroscopy) and its characterization prior to its first application to measure ^{6}Li+^{12}C nuclear reactions. Measurements were performed at the 3 MV tandem accelerator of the CNA (National Accelerator Center), in Seville, Spain. The ^{6}Li projectiles were accelerated at energies around the ^{6}Li+^{12}C Coulomb barrier ($V_B^{cm} \sim 3.0$ MeV - center of mass and $V_B^{lab} \sim 4.5$ MeV - laboratory frame). Using a $^{6}Li^{2+}$ beam, we measured at 13 laboratory energies from 4.00 to 7.75 MeV. Thus, we present the excitation function of $^{12}C(^{6}Li,^{4}He)^{14}N^{g.s.}$ reaction, at 2 backward angles (110.0° and 140.0°). The projectile dissociation, leading to this reaction, increases with the bombarding energies around the Coulomb barrier. This dissociation is favored at an optimum energy $E_b^{op} \geq V_B + |Q_{bu}|$, where V_B is the Coulomb barrier of the system, and $|Q_{bu}|$ is the module of Q-value for the ^{6}Li dissociation into ^{4}He+^{2}H. This result corroborates a systematic analysis of weakly bound projectiles reacting on several targets [1].

1 Introduction

First nuclei, isotopes of hydrogen (H) and helium (He), originated during primordial nucleosynthesis as a result of the big bang, with very low yield rates of exotic ^{7}Be and weakly bound stable ^{7}Li nuclei [2]. Heavier nuclei originated much later, during stellar nucleosynthesis, by nuclear reactions of lighter elements, from isotopes of hydrogen H (Z = 1) and helium He (Z = 2), in the stars' birth, life, and death. The latter with the consequent nucleosynthesis of heavier nuclei in supernovae events [3]. Thus, all matter known in the Universe originates from nuclear reactions. Measurements and analysis of nuclear reactions are key to understanding the yield rate and abundance of elements in the cosmos, the dynamics of stellar bodies, and the different Astrophysics scenarios [2–9].

Regarding the abundance of light elements in the cosmos, there is a gap between He and C, where the abundances of Li, Be and B elements are very low and the nuclei with masses A = 5 and A = 8 are not stable. The truth about such abundances must be related to the nuclei structure and reaction dynamics and their probability of being formed or dissociated in nuclear reactions.

Different works reported on Li nuclear reactions. For example, Pfeiffer and collaborators [10] reported on the cross section of the emerging ^{4}He (alpha particles), derived from ^{6}Li dissociation into ^{4}He and ^{2}H, peak at the grazing angle. Mayer and Schneider [11] established an energy threshold above which the Rutherford decrease is accompanied by a strong increase in the reaction cross section of ^{6}Li on ^{12}C, at bombarding energies below 5.50 MeV, analyzing the scattering angle at 165.0°. Capurro et al. reported the ^{6}Li breakup excitation function, at 170.0°, for the ^{6}Li+^{144}Sm system [12]. Luong and collaborators [13] reported the predominance of transfer reactions, at sub-barrier energies, in triggering the breakup of ^{6,7}Li reacting on ^{144}Sm and ^{207,208,209}Pb targets. Pandit et al. [14] determined the nuclear reaction t capture as dominant (∼70%) for the ^{7}Li+^{93}Nb. The systematic capture of t and the inclusive production of α (cross section) for reactions involving ^{7}Li, over a wide mass range, was also reported. The elastic scattering angular distributions of ^{6,7,9,11}Li impinging on ^{64}Zn, ^{120}Sn and ^{208}Pb heavy targets, at bombarding energies around the respective Coulomb barriers, have been previously analyzed [1, 15–17]. The systematic optical model (OM) analysis and the respective optical potentials (OP) were shown to strongly correlate with the projectile nuclear structure and its breakup probability. At an optimum bombarding energy, dependent on the Q-value of the projectile breakup and the Coulomb barrier of the system, the projectile tends to dissociate (through breakup and/or transfer reactions). This fact requires adapting the OM to the projectile structure. Stable tightly bound nuclei reactions require short-range Coulomb and nuclear potentials; weakly bound nuclei reactions require accounting for very strong short-range nuclear absorptive processes; and exotic nuclei reactions require short- and long-range Coulomb and nuclear

[a] e-mail: lgarrido2@us.es (corresponding author)

Published online: 07 May 2025

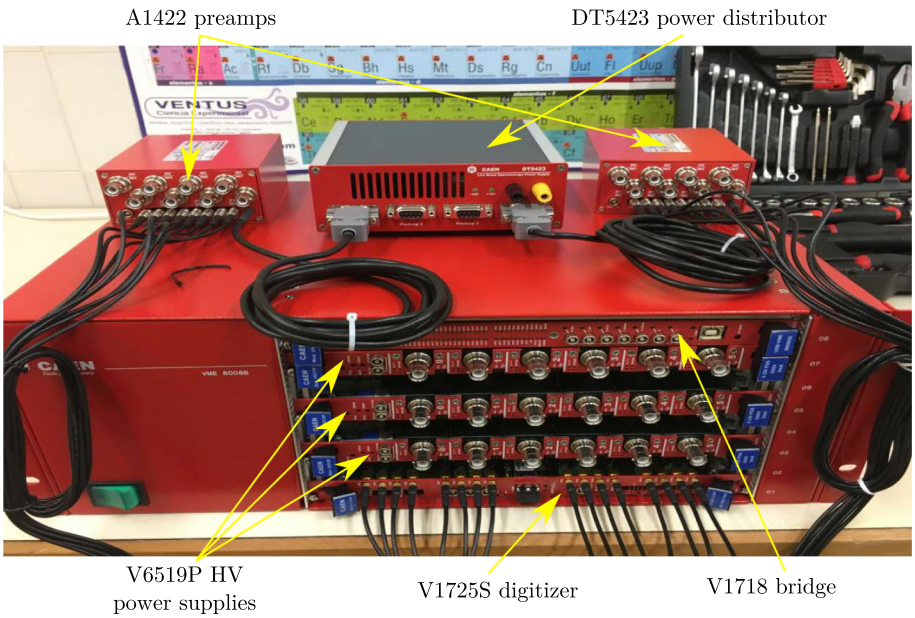

Fig. 1 MARS electronic system based on CAEN SpA desktop and VME modules

potentials, to account for extreme absorption processes, which extend to longer distances, far away from the nuclear short-range interaction [15–17].

In this context, we propose to investigate further the ^{6}Li nuclear reactions. We concentrate on the production of ^{4}He, derived from the dissociation of ^{6}Li into ^{4}He and ^{2}H, through breakup or transfer of ^{2}H (capture - incomplete fusion) to the ^{12}C, lighter target, that forms ^{14}N, in the ground and excited states. This investigation is proposed as a function of the bombarding energy and the detection angle. It completes and improves previous data [11, 18].

The MARS spectrometer benefits from the state-of-the-art in radiation detection, digital signal processing, and data acquisition. Today, this state-of-the-art links two main features: (i) the increasing use of digital techniques in processing pulses from detectors and (ii) the increasing trend of digitizing pulses closer to radiation detectors [19, 20]. Among the 3 major data acquisition standards used in nuclear and particle Physics, VME (VERSA module eurocard) [19] bus modules communicate through digital signals bussed over the backplane, and data transfer occurs by direct memory access. Within VME, the parameters are set through the software, allowing for automated control. The GUI (Graphical user interface) is located on an embedded computer within a VME bus module. Overcoming the limits of traditional analog acquisition chains, new waveform digitizers have been developed [21–25]. They consist of models that differ in sampling frequency, resolution, number of channels, form factor, and memory size. Further developments include DPP (Digital pulse processing) algorithms [26–29], installed in an FPGA (Field programmable gate array), allowing online analysis and new acquisition methods that go beyond the simple waveform record. Thus, a DPP-equipped digitizer provides a fully digital replacement for most traditional modules. Digitizers are available in VME and desktop form factors and represent the latest in pulse processing and data acquisition systems.

MARS integrates detection, electronic, and data acquisition in a very compact system. The electronic sub-system combines desktop (preamplifiers) and VME (digitizer, among other modules) form factors. MARS consists of 16 channels spectrometer for studying charged particles outgoing nuclear reactions.

In Sect. 2, we present MARS as a spectrometer. In Sect. 3, we present MARS characterization: (i) on a laboratory bench with emulated electronic pulses; (ii) coupled to a reaction chamber and a silicon detector irradiated by a radioactive triple alpha source; and (iii) coupled to a reaction chamber, placed in one of the experimental beam lines at the CNA [30], to measure ^{6}Li+^{12}C nuclear reactions. In Sect. 4, we present the first results of the application of MARS to the ^{6}Li+^{12}C measurements. Finally, in Sect. 5, we draw our main conclusions.

2 MARS description

MARS (Modular apparatus for nuclear reactions spectroscopy) is a compact and portable spectrometer that can measure the angular and energy distributions of charged particles emerging from nuclear reactions. Its design allows different types of digitizer, firmware, and then acquisition systems to be applied. In particular, the different firmware allows for different pulse analysis techniques.

MARS detection system is composed of 16 totally depleted silicon (Si) SBD (surface barrier detectors) from ORTEC with active areas of 50 mm^2. Eight of them have 15 μm thickness (model ED-35-050-15) (commercial value), which are named by their serial number (899–906). The other eight have 500 μm thickness (Model TB-15-050-500) and are also named according to their serial

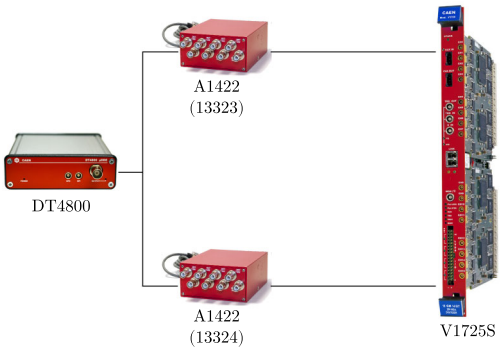

Fig. 2 Setup used for MARS characterization using the DT4800 emulator

number (52–59). Thus, MARS allows one to coupling 8 Si telescopes. These detectors, in single or telescope configurations, are suitable for charged-particle identification and their respective high-resolution spectroscopy. The manufacturer specifies resolutions, respectively, of 35 keV (15 μm) and 15 keV (500 μm), for ^{241}Am alphas (5.486 MeV (85% of intensity)) [31, 32]. The efficiency of Si SBD detectors, for medium- to high-energy particles, is commonly assumed to be at unity ([33] and references therein). A simple Monte Carlo simulation performed with SRIM [34], considering the ^{241}Am alpha particles, with 5.486 MeV, at incident angle of 0°, shows that less than 0.01% are backscattered.

Figure 1 shows MARS electronic system. It combines desktop and VME modules from the CAEN SpA company. It consists of two charge sensitive A1422 preamplifiers [35], one DT5423 power distributor [36], three V6519P HV power supply modules [37], one V1725S digitizer [38] and one V1718 bridge [39]. The V6519P, V1725S and V1718 modules are connected in an 8 slot VME crate VME8008B [40]. The V1725S digitizer runs the DPP - PSD (Pulse shape discrimination) or DPP - PHA (Pulse height analysis), firmware. Event selection can be performed using a LED (leading edge discriminator) or a CFD (constant fraction discriminator). The PHA firmware allows the digitizer to obtain an energy spectrum by applying a trapezoidal filter to the input pulse and is suitable for processing pulses with long decay times, such as those produced by alphas and heavy ions in semiconductor detectors [41]. The 16 channels V1725S digitizer is ideal for working with 16 silicon detectors. In particular, their association allows for coupling 8 telescopes, the respective coincidence measurements and data acquisition. Finally, a PC handles the data acquisition from the V1725S digitizer by means of CoMPASS (CAEN Multi-PArameter Spectroscopy Software) [41].

3 MARS characterization

As a proof-of-concept, prior to its first application, MARS has been tested in a laboratory environment. Figure 2 schematizes the first setup used to characterize the MARS electronic system. The test pulses were generated by the 419 ORTEC precision pulse generator [42] or the digital detector emulator DT4800 [43]. The DT4800 (Fig. 2) can generate random pulses that emulate radiation sources (for example, a triple alpha source) and detector signals, with the respective energy and time distributions.

According to Fig. 2, MARS system is divided into 8 individual electronic chains (1–8) related to each 8 channels A1422 (13323 and 13324) preamplifier and 16 data acquisition (DAQ) chains (0–15) related to the V1725S digitizer.

The pulse height and time response of the two preamplifiers have been characterized using the pulse generator. For a precise calibration proposal, individual amplification factors (F) have been determined for each A1422 channel. For comparison, the mean values of $\overline{F} = 1.075\ (34)$ and 1.084 (39) were obtained, respectively, for the modules A1422-13323 and 13324.

For both A1422 modules, the rise time is $t_r^{out} \approx 13$ ns (for input pulses with fast rise times $t_r^{in} < 15$ ns), which is in agreement with the data sheet value ($t_r^{out} < 25$ ns). For long input pulses ($t_d^{in} > 1.5$ ms), the output decay time remains constant at $t_d^{out} \approx 46$ μs, which can be compared to the data sheet value ($t_d^{out} = 50$ μs).

The maximum pulse height digitized by MARS is 1.7(1) V. The uncertainty takes into account differences related, for example, to the A1422 amplification factors (F). These voltage values correspond to energies of 19(1) MeV, according to the sensitivity of 90 mV/MeV of A1422, given by the data sheet [35].

Using DT4800 (Fig. 2), we determined the relation between the input pulse height and the spectrum channel. With emulated spectra, processed by each of 16 electronic / acquisition chains, we were able to guarantee the MARS linearity. It was further verified with a triple alpha radioactive source (Sect. 3.1) and during the nuclear reaction experiment (chapter 4).

We estimated the dead time of the system by transmitting constant pulses at different frequencies. CoMPASS calculates the dead time percentage using equation (1):

$$1 - \frac{O + U + S}{I} \tag{1}$$

where O is the number of output events, U is the number of user-discarded events, S is the number of saturation events, and I is the number of input events. We observed that increasing the input frequency from 10^2 to 10^3 Hz increases the dead time from 0.2%

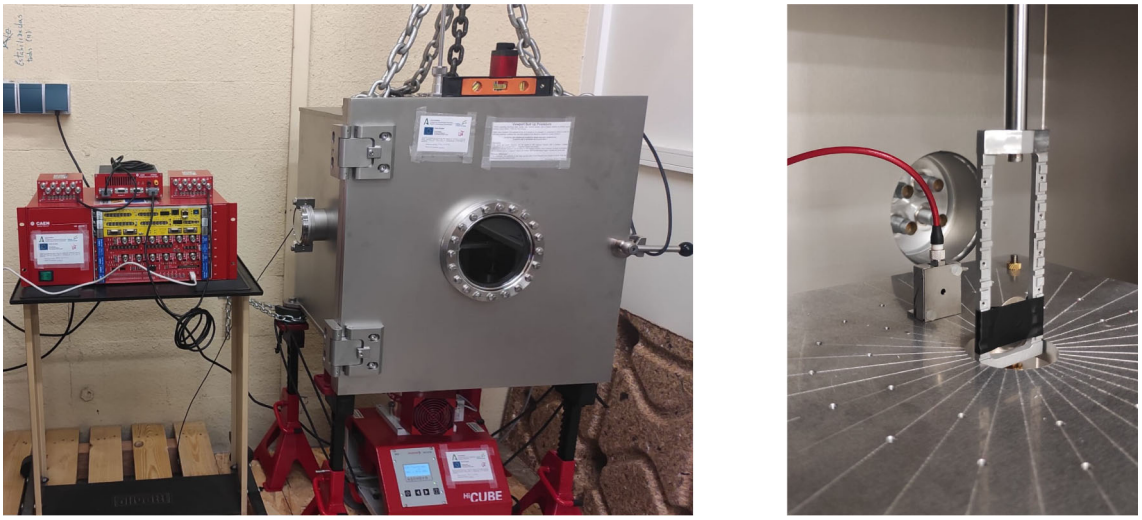

(a) MARS electronics connected to the vacuum chamber. (b) view inside the chamber.

Fig. 3 MARS (left) coupled to a vacuum chamber (in the middle) with a triple alpha source, in front of a Si detector (right), to study the spectral response of the system

Table 1 The energies and intensities of the main radioactive triple alpha source emissions

Isotope	Energy (MeV)	Intensity (%)
^{233}U	4.729	1.6
	4.783	13.2
	4.824	**84.3**
^{239}Pu	5.106	11.9
	5.144	17.1
	5.157	**70.8**
^{241}Am	5.388	1.7
	5.442	13.1
	5.486	**84.8**

The most instense emissions are identified in bold

to 1.1%, and increasing the frequency from 10^3 to 10^4 Hz increases the dead time from 1.2% to 11.6%. Thus, for nuclear reaction measurements, this property must be under control for optimizing the counting rate.

The DT4800 (in Fig. 2) has also been applied to verify the resolution for different emulated pulse heights. With the DT4800, we emulated a spectrum of a triple alpha source composed of ^{239}Pu (5.15 MeV), ^{241}Am (5.48 MeV) and ^{244}Cm (5.80 MeV). The resolution values obtained vary from $R = 0.12\%$ to $R = 0.14\%$. It allows for resolving typical triple alpha peaks, between 4 and 6 MeV, of which the main peaks are separated by ~ 300 keV.

This characterization process was carried out considering the maximum number of V1725S digitizer acquisition channels ($2^{14} = 16384$ channels). It should be mentioned that most of the values presented here go beyond data sheets, being crucial for a precise calibration, counting rate optimization and/or particle identification proposals.

3.1 Triple alpha source measurements

3.1.1 Laboratory equipment and setup

To validate MARS in a relevant controlled environment, we used the vacuum chamber located in the Applied Laboratory On Heavy-ions Analysis (ALOHA), at the Department of Atomic, Molecular and Nuclear Physics of the University of Seville (Fig. 3).

3.1.2 Resolution of 500 μm Si SBD

Next tests aim to determine the resolution of the thicker (500 μm) detectors. For this, we used a real triple alpha source composed of ^{233}U, ^{239}Pu, and ^{241}Am. The energies and intensities of the main alpha emissions are presented in Table 1.

Figure 4 shows a typical triple alpha (^{233}U, ^{239}Pu, and ^{241}Am) spectrum. With spectra obtained for all individual detectors, we verified the linearity of MARS and studied the detector resolution. As expected, the main (triple) alpha peaks, between 4 and 6 MeV,

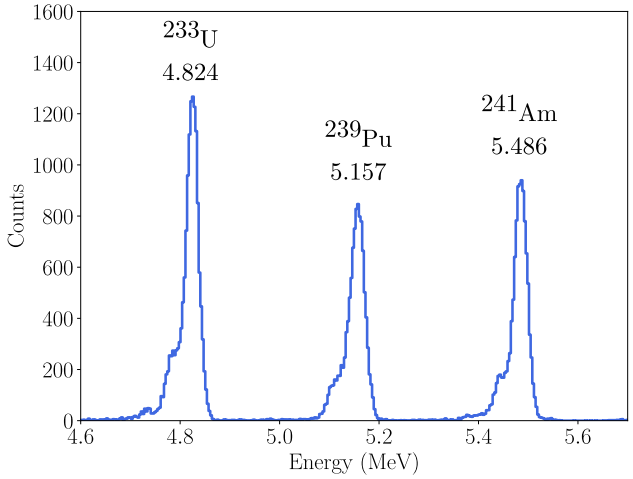

Fig. 4 Typical triple alpha source spectrum, related to Table 1, measured with MARS

separated by ∼300 keV, are very well resolved. In Fig. 4, the peaks are slightly asymmetric (to the left) due to other decay modes (see Table 1) with lower yields and lower energies (from 10 to 100 keV), with respect to the main peaks. In Fig. 4, the full width at half maximum (FWHM) of the three main peaks are, respectively, 32, 39 and 36 keV and the resolutions $R(\%)$ are 0.67%, 0.74% and 0.60%.

For the sake of comparison, the PHA parameters were kept constant for all chains. Thus, we achieved resolutions ranging from 0.7% to 2.2%. By individually fine-tuning the PHA parameters, we were able to improve the resolutions below 2.0%, getting, on average, much closer to 1.0%. It is the case of the triple alpha source results presented above and illustrated by Fig. 4. These adjustments tend to decrease fluctuations between detectors and the different electronic/acquisition chains. The resolution pattern validates MARS for applications in nuclear reactions.

3.1.3 Experimental thickness of 15 μm Si SBD

The 15 μm thick (commercial value) of Si SBD represents the technological limit in terms of thickness. This limit implies accentuated thickness variations and therefore uncertainties that must be quantified. The detector thickness determination is mandatory to allow telescope ($\Delta E + E$) configuration, coincidence measurements, as well as the consequent spectroscopy and identification of charged particles.

The linear stopping power S for charged particles in silicon is defined as the particle differential energy loss within Si divided by the differential path length:

$$S = -\frac{\mathrm{d}E}{\mathrm{d}x} \tag{2}$$

The total energy deposited (ΔE) at the path length can be expressed by:

$$\Delta E = \int_0^t \frac{\mathrm{d}E}{\mathrm{d}x}\mathrm{d}x' \tag{3}$$

where t represents the Si thickness. The Bethe formula classically describes the specific energy loss as a function of the fragment charge:

$$-\frac{\mathrm{d}E}{\mathrm{d}x} = \frac{4\pi e^4 z^2}{m_0 v^2} N B \tag{4}$$

where

$$B = Z\left[\ln\frac{2m_0v^2}{I} - \ln\left(1-\frac{v^2}{c^2}\right) - \frac{v^2}{c^2}\right] \tag{5}$$

being v the velocity of the incoming particle, ze its charge, N represents the number density, Z is the atomic number of Si (in this case), m_0 is the electron rest mass, e is the electronic charge, I is the average excitation and ionization potential of the Si and c is the velocity of light in the vacuum. For non-relativistic ($v << c$) charged particles, only the first term of B is significant [20].

According to the Bethe formula and the telescope configuration, different charged particles lose different amounts of energy passing through the forward thinner detector. A typical spectrum (ΔE versus E_{total}, with E_{total}=$\Delta E + E$) allows for charge separation and identification. In addition, the detector thickness will determine which particles stop in the first (forward) detector and which do not (passing through and leaving the remaining energy in the second (backward) detector). Thus, thickness determination is a key step in the characterization of the detection system.

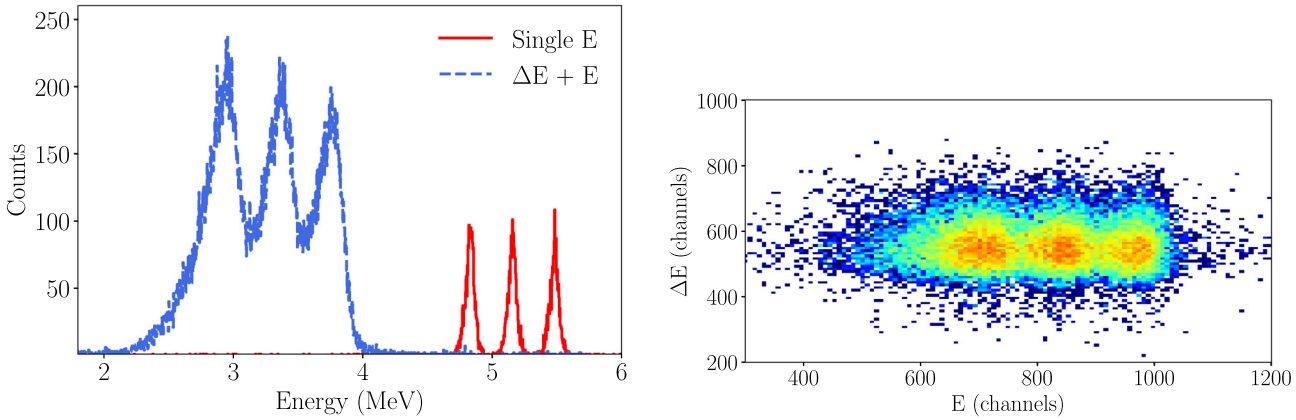

(a) One-dimensional (1D) triple alpha spectra obtained with a single thick (E) detector (right) and (ΔE+E) telescope (left). The energy shift of the peaks depends on the thickness of the thin (ΔE) forward detector.

(b) Two-dimensional (2D) triple alpha spectrum obtained with a telescope configuration. The three main peaks can be identified.

Fig. 5 Typical triple alpha spectra obtained with single and telescope configurations

Table 2 Nominal (from detectors data sheet) and measured thicknesses of the thin 15 μm (commercial value) detectors

Detector	Nominal thickness (μm)	Measured thickness (μm)
899	8.0	9.4(4)
900	8.0	11.5(1)
901	14.8	14.2(1)
902	14.6	14.4(3)
903	14.0	13.7(2)
904	14.7	14.5(3)
905	10.4	9.6(2)
906	10.4	10.0(1)

Using the same radioactive triple alpha source (^{233}U, ^{239}Pu, and ^{241}Am), we determined experimentally the thicknesses of the Si detectors by measuring the energy deposition (ΔE) of the alpha particles in a telescope.

The results are presented in Table 2 and compared to the respective nominal thickness value obtained from each detector data sheet.

As a procedure, we first acquired a spectrum using a single thick (500 μm) Si detector (see Fig. 5a on the right/red solid line). Then, we acquired coincidence (logic AND) spectra (Fig. 5a) on the left/dashed blue line and Fig. 5b) from a (ΔE+E) telescope. For completeness and to demonstrate the capability of the system, Fig. 5b shows the 2D spectrum.

Figure 5a shows how the alpha peaks are shifted to the left when placing the thin Si detector in front of the thick one. In this case, the shift (ΔE) is, respectively, 1.88, 1.79, and 1.72 MeV. As expected, according to the Bethe formula, the lower the incident energy, the higher the energy loss. Measurements were performed with a collimator with 2 mm diameter placed between the source and the detector/telescope.

The stopping power (S) for alpha particles, in silicon, was obtained from SRIM (Stopping and range of ions in matter) [34]. According to equation (3), to obtain the experimental thicknesses (t), the stopping power (S) is integrated in steps dx, until the measured ΔE is reached. The sum of the steps provides the final value of t.

In Table 2, the nominal thickness (data sheet of each individual detector) ranges from 8.0 to 14.8 μm. According to the manufacturer, the sensitive depth (minimum) can vary from 7 to 15 μm. In Table 2, each nominal (absolute) thickness value can be compared with the experimental value (within its uncertainty). The mean nominal (absolute) value is $\bar{t} = (11.9 \pm 3.0)$ μm, assuming the standard deviation (1σ). It implies a relative error of 25%. The measured thickness ranges from 9.4 to 14.5 μm. The respective mean value is $\bar{t} = (12.2 \pm 2.3)$ μm, assuming the standard deviation (1σ). It implies a relative error of 19%. These nominal and measured mean thicknesses differ, respectively, 21% and 19% from the commercial value (15.0 μm).

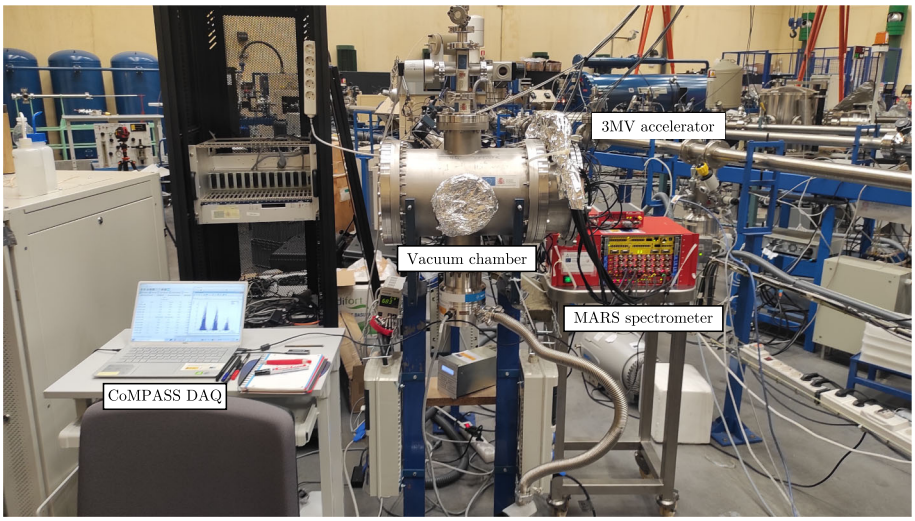

Fig. 6 MARS coupled to the 3 MV tandem accelerator, at the CNA, in Seville (Spain)

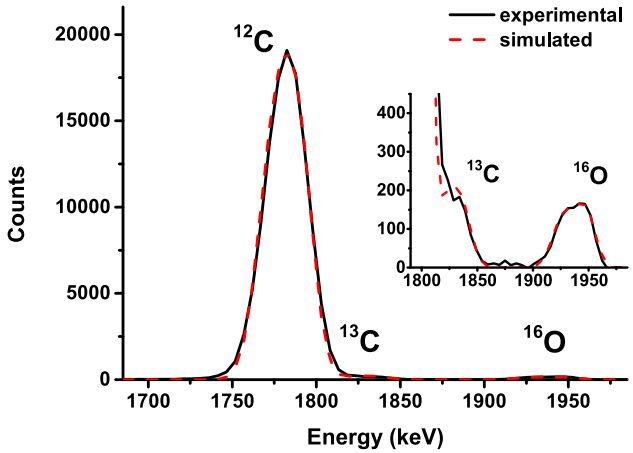

Fig. 7 p-EBS spectrum of protons beam on C target, at 2.50 MeV and 165.0°

3.2 Beam test: nuclear reaction setup

In order to validate MARS in an operational environment, a nuclear reaction experiment was proposed. The main goal was to measure the ^{6}Li+^{12}C collision at the 3 MV tandem accelerator of the CNA (National Accelerators Center), in Seville, Spain (Fig. 6). For the current study, we are most interested in the reactions that lead to the dissociation of ^{6}Li into its cluster components, ^{4}He+^{2}H. For instance, the pure breakup of ^{6}Li resulting on ^{12}C+^{4}He+^{2}H with a $Q_{\text{value}} = -1473.7$ keV; deuteron transfer (capture) resulting on ^{14}N+^{4}He, with a $Q_{\text{value}} = 8798.58$ keV, and the ^{4}He transfer (capture) resulting on ^{16}O+^{2}H, with a $Q_{\text{value}} = 5688.18$ keV, as a competitive reaction channel.

The experiment was carried out in the reaction chamber of the BNP (Basic Nuclear Physics) line, located at the end of the +30° exit of the accelerator.

The carbon (C) target was characterized in the same facility by p-EBS (proton Elastic Backscattering Spectroscopy), using a 2.5 MeV proton beam and a PIPS (Passivated Implanted Planar Silicon) detector set at 165.0°.

Figure 7 shows the spectrum due to 3 different target components: C (^{12}C, ^{13}C) and O (^{16}O). This spectrum, simulated by SIMNRA [44] (using the natural isotopic abundance), results in the mass density of each isotope: 115(2) μg/cm^2 for carbon (C) and 1.5(1) μg/cm^2 for oxygen (O). Finally, for normalization purposes, a thin layer ($\sim$ 14 μg/cm^2) of ^{197}Au was evaporated on the target.

Figure 8 shows the experimental setup inside the reaction chamber. A double-collimator system is installed in the entrance of the reaction chamber, on the same detectors base, just in front of the target. Thus, the beam is aligned and collimated, which guarantees the impact of the beam on the center of the target. Before colliding the ^{6}Li beam with the ^{12}C target, it was previously projected on a scintillator material (see Fig. 8, on the left). Thus, the beam was centered on the target and its current was optimized. Figure 8 (in the middle) shows the target holder with the above-mentioned scintillator and the ^{12}C target. The target is surrounded by Si detectors (Fig. 8, on the right). A similar double-collimator system is installed in front of each silicon detector/telescope. To normalize the response of the detection system, elastic scattering of the ^{6}Li on the ^{197}Au (evaporated on the ^{12}C target) was measured. In the

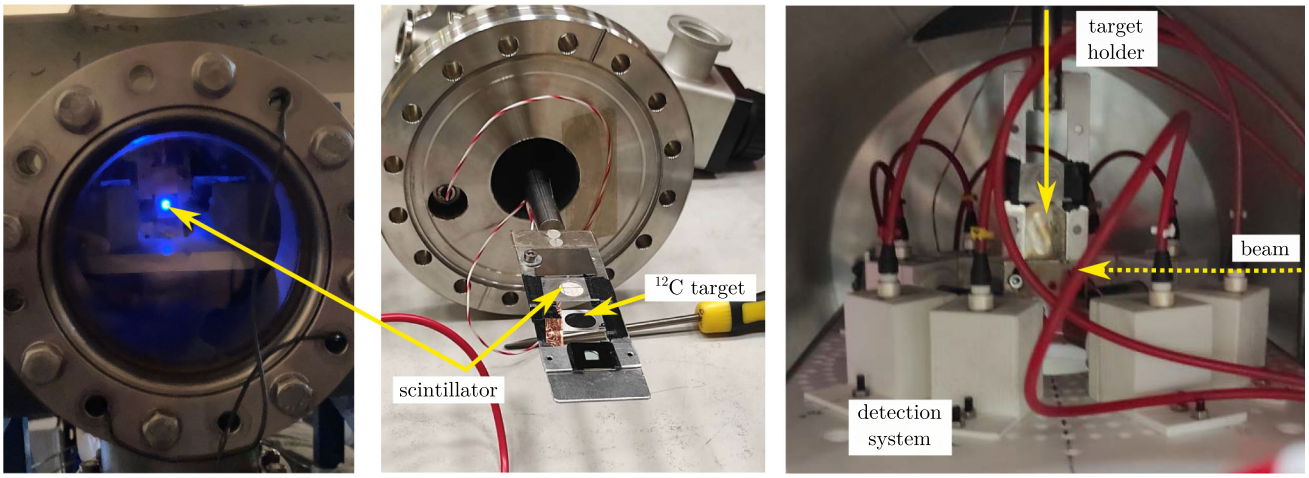

Fig. 8 Target holder and detection system placed into the vacuum reaction chamber

energy range, Rutherford behavior, $1/sin^4(\theta_{c.m.}/2)$, is expected for the entire angular range. Thus, the geometry of the setup can be fully checked, and the solid angles are calculated for each detector based on their distances to the target and laboratory angles.

4 Results on ^{6}Li+^{12}C nuclear reactions

The first measurement was carried out with an incident beam energy of $E_{\text{lab}} = 6.00$ MeV, which is above the Coulomb barrier ($V_B^{\text{lab}} \sim 4.5$ MeV), for ^{6}Li+^{12}C system. For this, we used ^{6}Li^{2+} beam accelerated by a terminal voltage of $V_T = 2.0$ MV. The detectors were mounted in single and telescope configurations. Following dead time constraints, the intensity (current) of the incoming beam was around 20 nA, with a maximum counting rate of the order of 1 kHz in the detectors, which implies in $\sim 1.5\%$ dead time.

Figure 9 shows ^{6}Li+^{12}C nuclear reaction spectra, measured at 6.00 MeV and 35.0°. This angle was chosen for statistical reasons.

Figure 9a shows a one-dimensional (1D) spectrum of the ^{6}Li+^{12}C reaction. Here, several nuclear reaction peaks can be identified. Most of the identified peaks are related to the ^{12}C(^{6}Li,^{4}He)^{14}N* reaction, from which alpha particles (^{4}He) are detected and completely stopped by the single thicker Si detectors. One of the peaks identified in the 1D spectrum is produced by the elastic scattering of ^{6}Li on ^{16}O (a target contaminant, determined by p-EBS analysis). Another wide peak, centered at ≈ 3.1 MeV, is produced by the recoil of ^{12}C and ^{16}O from the target. In Fig. 7, we observe the ^{16}O contaminant that, in addition to the ^{12}C (main target component) and according to the simulations of SIMNRA [44] should (both) contribute to such a wide peak.

Figure 9b shows a two-dimensional (2D) spectrum (ΔE+E) of the ^{6}Li+^{12}C reaction, measured at 6.00 MeV and 35.0°. Here, different spots (areas) can be identified. Most of the identified spots are (energy) correlated with alpha particles coming from the ^{12}C(^{6}Li,^{4}He)^{14}N* reaction.

Figure 9c shows one-dimensional (1D) spectrum of ^{6}Li+^{12}C reaction, measured at 6.00 MeV and 35.0° (the same as in Fig. 9a). In addition, superimposed on it, we present the projection of alpha particles, observed in Fig. 9b, on the total energy ($\Delta E + E$) axis. Thus, we were able to energetically correlate the spots (areas) of Fig. 9b with identified peaks of Fig. 9a. It is worth mentioning that higher energy alphas are not visible in the 2D spectrum because they deposit a negligible amount of energy in ΔE, which is below the threshold.

Therefore, with MARS, in single or telescope configuration, we can discriminate several peaks related to the ^{12}C(^{6}Li,^{4}He)^{14}N nuclear reaction.

As an example, in the single (1D) spectrum of Fig. 9, the resolution obtained from the peak related to the ^{12}C(^{6}Li,^{4}He)^{14}N$^{g.s.}$ (alpha particles correlated with the ^{14}N ground state as output reaction channel) is 2.1%.

Further measurements have been carried out, which allow obtaining excitation functions for ^{6}Li+^{12}C nuclear reactions. The complete set of measurements consists of 13 bombarding energies: 4.00, 4.50, 5.00, 5.50, 5.75, 6.00, 6.25, 6.50, 6.75, 7.00, 7.25, 7.50, 7.75 MeV; with detectors mounted at 8 angles: 35.0, 40.0, 65.0, 70.0, 110.0, 115.0, 140.0, and 145.0°. Due to collimation and the respective solid angles, two consecutive angles are compatible within the angular precision ($\theta \pm 2.5°$). The nuclear effects are supposed to be pronounced at the rear angles. Figure 10 shows a 1D spectrum related to ^{6}Li+^{12}C reactions, measured at 6.00 MeV, with the detector at 110.0°. A quite similar resolution pattern is observed when comparing the single spectra obtained at the forward angle (35.0°) and at the backward angle (110.0°). In both cases, the ^{12}C(^{6}Li,^{4}He)^{14}N$^{g.s.}$ peak is very well resolved, without background. Due to this resolution pattern and to detect high-energy alpha particles, measurements were carried out with the 8 thicker (500 μm) Si detectors, in a single configuration. Thus, we investigate the ^{12}C(^{6}Li,^{4}He)^{14}N$^{g.s.}$ reaction and its respective cross section, as a function of the bombarding energy. Data were taken with the aim of reducing the statistical uncertainties below

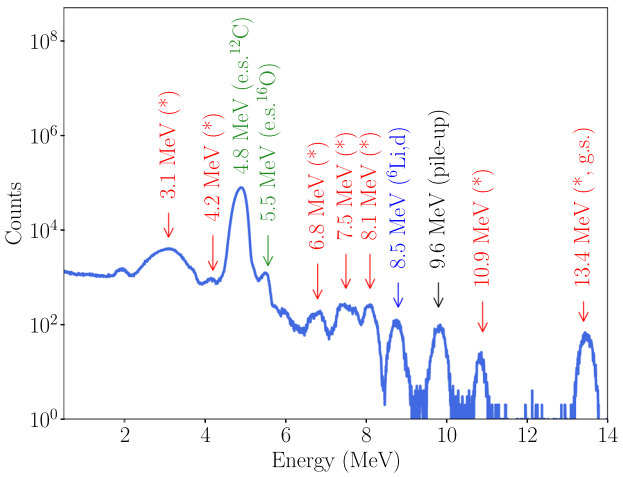

(a) One-dimensional (1D) spectrum of ^{6}Li+^{12}C reaction. Theoretical values of alpha particles kinetic energy, coming from ^{12}C(^{6}Li,^{4}He)^{14}N, are highlighted with an asterisk. The elastic scattering (e.s.) of ^{6}Li on ^{12}C and ^{16}O are also identified as well as a possible pile-up related to the former and deuterons coming from ^{12}C(^{6}Li,d)^{16}O$^{g.s.}$.

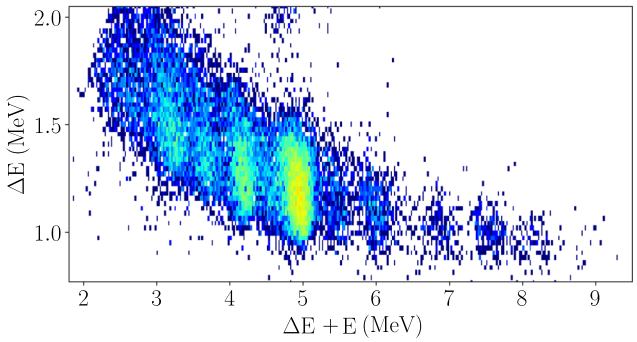

(b) Two-dimensional (2D) spectrum of alpha particles coming mainly from ^{12}C(^{6}Li,^{4}He)^{14}N* reaction. The coincidence window was optimized (in terms mainly of dead time) and set to 192 ns.

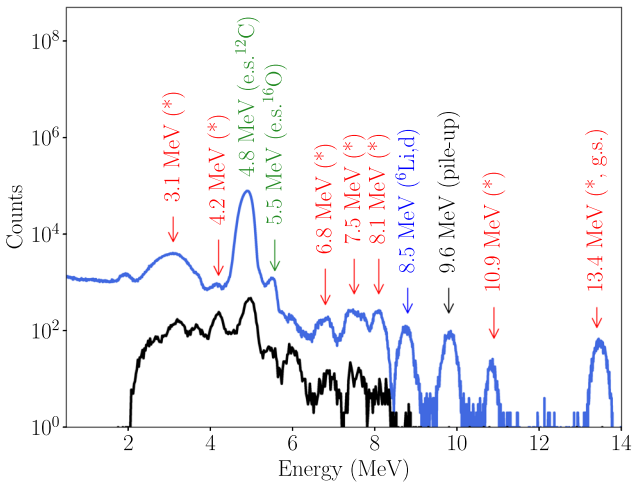

(c) 2D spectrum (b) projected on 1D ones (a).

Fig. 9 1D and 2D spectra for the ^{6}Li+^{12}C reaction measured at 6.00 MeV and 35.0°

5%. Thus, the number of counts (N) related to the ^{12}C(^{6}Li,^{4}He)^{14}N$^{g.s.}$ peak, for all angles and energies, is mainly greater than 500 counts (see, for example, Figs. 9 and 10). The statistical error is then calculated as a function of $1/\sqrt{N}$, resulting in the error bars presented in Fig. 11. There is also an angular uncertainty related to the detectors' position. However, it decreases with the angle of scattering (according to the Rutherford scattering dependence with $1/sin^4(\theta_{c.m.}/2)$), and it is negligible compared to the statistical uncertainty at the backward angles.

Figure 11 shows two excitation functions obtained at two angles (110.0° and 140.0°). For both excitation functions, we observe a continuous increase in the ^{12}C(^{6}Li,^{4}He)^{14}N$^{g.s.}$ reaction cross section, from the bombarding energies around the Coulomb barrier ($V_B^{\text{lab}} \sim 4.5$ MeV). A pronounced increase in the reaction cross sections is observed, from ~ 6.00 MeV (vertical dashed line) to a peak at ~ 6.75 MeV. In fact, a variation of one order of magnitude is observed from below the Coulomb barrier ($V_B^{\text{lab}} \sim 4.5$ MeV) to $E_b^{\text{op}} \sim 6.75$ MeV. This effect is better observed at 110.0°, where ^{12}C(^{6}Li,^{4}He)^{14}N$^{g.s.}$ is resolved for the complete set of energies. The optimal energy (E_b^{op}), of ^{6}Li dissociation, is in good agreement with our prediction $E_b^{\text{op}} \geq V_B + |Q_{bu}|$, where, V_B is the Coulomb barrier of the system ($V_B^{\text{lab}} \sim 4.5$ MeV); and $|Q_{bu}|$ is the module of the Q-value for the dissociation of ^{6}Li into its

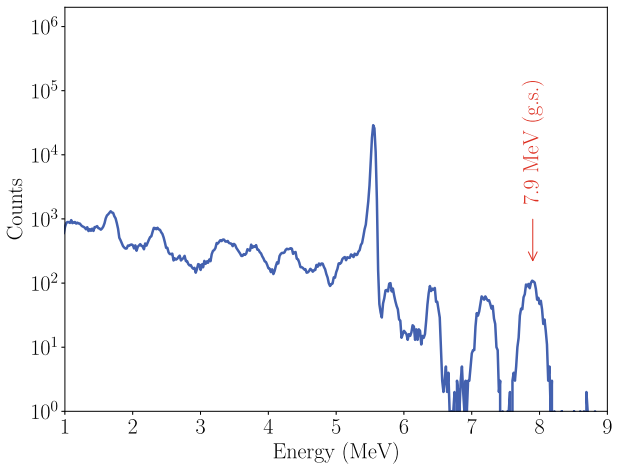

Fig. 10 One-dimensional (1D) spectrum of ^{6}Li+^{12}C,^{197}Au reaction at 6.00 MeV and 110.0°. The arrow points out the value of the alpha particles kinetic energy, coming from ^{12}C(^{6}Li,^{4}He)^{14}N$^{g.s.}$

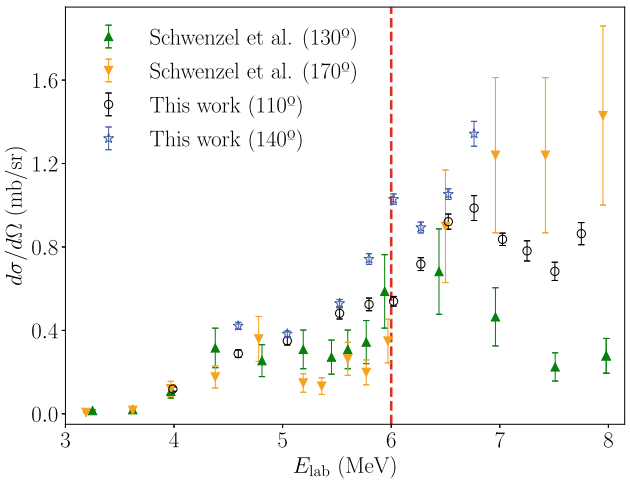

Fig. 11 Excitation functions of the ^{12}C(^{6}Li,^{4}He)^{14}N$^{g.s.}$ reaction at 110.0° and 140.0° obtained in this work and its comparison to the results at 130.0° and 170.0° from [18]

cluster components ^{4}He+^{2}H ($|Q_{bu}|\sim$ 1.5 MeV). This result, even obtained for one specific nuclear reaction channel, agrees and helps to corroborate previous recent results published in [1, 45].

In Fig. 11, we also compare the current data with the previous data obtained in [18]. The current manuscript presents measurements at two different angles (110.0° and 140.0°), with a greater number of experimental points (energy precision) and better statistics (reaction cross-section precision). In particular, at 110.0°, we obtained a better defined peak structure, for the reaction cross-section values, around $E_b^{\text{op}} \sim 6.75$ MeV, which is, in general, due to the better precision of the current data.

5 Conclusions

This work introduces the MARS spectrometer that combines the thinnest (15 μm) technology of silicon detectors with the state-of-the-art VME digitizer with DPP-PSD/PHA firmware. MARS validation included 3 phases: (i) laboratory bench; (ii) relevant environment; and (iii) operational environment.

For the first phase (laboratory bench) of MARS validation, we used the 419 ORTEC precision pulse generator [42] and the emulator DT4800 [43]. The signals were processed through the electronic scheme presented in Fig. 2 and acquired with CoMPASS.

For the second phase (relevant environment) of MARS validation, we used a triple alpha radioactive source, made of ^{233}U, ^{239}Pu and ^{241}Am. It was placed in a vacuum chamber, facing the silicon detectors (Fig. 3). The resolution (R) of the thicker detectors (500 μm) presented a variation from 0.7% to 2.2%. Further improvements ($R < 2.0\%$) were achieved by setting individual PHA parameters, for different chains (detection, electronic, and acquisition). For thinner detectors, the commercial thickness value (15.0 μm) must be taken with caution. The nominal thicknesses (data sheet) and measured ones have variations of 25% and 19%, represented by their mean values $\bar{t} = (11.9 \pm 3.0)$ μm and $\bar{t} = (12.2 \pm 2.3)$ μm. Thus, the two absolute average values differ, respectively, 21% and 19% from the commercial ones. Such an individual characterization is mandatory for precise nuclear reaction spectroscopy and identification of charged particles.

For the third phase (operational environment) of MARS validation, we proposed measuring a nuclear reaction (^{6}Li+^{12}C), at the 3 MV tandem accelerator of the National Accelerator Center (CNA), in Seville, Spain. MARS allowed identifying several peaks related mainly to the ^{12}C(^{6}Li,^{4}He)^{14}N nuclear reaction. Results based on one-dimensional (1D) and two-dimensional (2D) spectra corroborate each other.

In this work, we concentrated on analyzing ^{12}C(^{6}Li,^{4}He)^{14}N$^{g.s.}$ cross sections. Thus, two excitation functions of ^{12}C(^{6}Li,^{4}He)^{14}N$^{g.s.}$ are reported, at two different backward angles (110.0° and 140.0°). The dissociation of the projectile is favored at bombarding energies above the Coulomb barrier and is accentuated at an optimum energy that peaks as a function of the Q-value of the projectile breakup and the Coulomb barrier of the system. This result complements and improves the previous ones obtained in [18] and, together with [12, 45], tends to corroborate the systematic analysis presented by [1].

New experimental campaigns are in development. The goal is to study weakly bound nuclei (for example, ^{6,7}Li, ^{9}Be, ^{10}B) reactions on different targets, above the Coulomb barrier, and around the optimal energy of weakly bound nuclei dissociation ($E_b^{\text{op}} \geq V_B + |Q_{bu}|$). New measurements confirm our prediction for the maximum energy of the weakly bound projectile dissociation at this specific energy. Measurements around it will confirm a systematic behavior for weakly bound nuclei and a way to further study the dynamics of their reactions as a function of their structures.

Acknowledgements The authors thank the particle accelerator operators, Ángel Jesús Romero Serrano and David Pascual Álvarez, for their contributions and dedication to ensure the successful operation of the facility. This work has been funded by the EQC2019-005873-P project, through the Spanish national subprogram for research infrastructure and scientific-technical equipment (national plan R+D+I 2017-2020). Within this framework, MARS has been developed in collaboration with private companies ATI Sistemas S. L. (by a signed contract between ATI Sistemas S. L. and the University of Seville) and CAEN (*Costruzioni Apparecchiature Elettroniche Nucleari*) SpA providing technical support. This work was partially supported by the Spanish Ministerio de Economía y Competitividad and FEDER funds (PGC2018-096994-B-C21) by the project PAIDI 2020, reference P20_01247, funded by the Consejería de Economía, Conocimiento, Empresas y Universidad, Junta de Andalucía (Spain) and "ERDF A way of making Europe", and the project PID2021-123879OB-C21 (with grant PRE2022-102551) funded by the Spanish Ministerio de Ciencia e Innovación. This work is also part of the project supported by the Spanish Ministerio de Ciencia, Innovación y Universidades (PID2023-146401NB-I00). This work has been developed within the context of IReNA (*International Research Network for Nuclear Astrophysics*) and IANNA (*Ibero-American Network of Nuclear Astrophysics*). The authors acknowledge all support and collaboration from IReNA and IANNA (National Science Foundation under Grant No. OISE-1927130).

Funding Funding for open access publishing: Universidad de Sevilla/CBUA.

Data availibility Data are available on request from the corresponding author. The manuscript has associated data in a data repository.

References

1. L. Garrido-Gómez, A. Vegas-Díaz, J.P. Fernández-García, M.A.G. Alvarez, Systematic optical potentials for reactions with cluster-structured nuclei. Phys. Rev. C **109**(5), 054608 (2024). https://doi.org/10.1103/PhysRevC.109.054608
2. R.A. Alpher, H. Bethe, G. Gamow, The origin of chemical elements. Phys. Rev. **73**, 803–804 (1948). https://doi.org/10.1103/PhysRev.73.803
3. E.M. Burbidge, G.R. Burbidge, W.A. Fowler, F. Hoyle, Synthesis of the elements in stars. Rev. Mod. Phys. **29**, 547–650 (1957). https://doi.org/10.1103/RevModPhys.29.547
4. E. Rutherford, Collisions of α particles with light atoms. IV. An anomalous effect in nitrogen. Phil. Mag. (2010). https://doi.org/10.1080/14786431003659230
5. F. Hoyle, D.N.F. Dunbar, W.A. Wenzel, W. Whaling, A state in C-12 predicted from astrophysical evidence. Phys. Rev. **92**, 1095 (1953)
6. F. Hoyle, On nuclear reactions occuring in very hot stars. I. The synthesis of elements from carbon to nickel. Astrophys. J. Suppl. Ser. **1**, 121 (1954). https://doi.org/10.1086/190005
7. K. Lodders, Solar system abundances and condensation temperatures of the elements. Astrophys. J. **591**(2), 1220–1247 (2003). https://doi.org/10.1086/375492
8. M. Chaussidon, F. Robert, K.D. McKeegan, Li and B isotopic variations in an Allende CAI: Evidence for the in situ decay of short-lived 10Be and for the possible presence of the short-lived nuclide 7Be in the early solar system. Geochim. Cosmochim. Acta **70**(1), 224–245 (2006). https://doi.org/10.1016/j.gca.2005.08.016
9. A. Bauswein, R. Pulpillo, H.T. Janka, S. Goriely, Nucleosynthesis constraints on the neutron star-black hole merger rate. Astrophys. J. Lett. (2014). https://doi.org/10.1088/2041-8205/795/1/L9
10. K.O. Pfeiffer, E. Speth, K. Bethge, Break-up of 6Li and 7Li on tin and nickel nuclei. Nucl. Phys. A **206**, 545–557 (1973). https://doi.org/10.1016/0375-9474(73)90084-5
11. M. Mayer, M. Schneider, Scattering cross-sections for 6Li and 7Li ions from carbon below 5.5 MeV. Nucl. Instrum. Methods B **183**(3), 221–226 (2001). https://doi.org/10.1016/S0168-583X(01)00768-6
12. O.A. Capurro, A.J. Pacheco, A. Arazi, J.M. Figueira, D. Martinez Heimann, A.E. Negri, Breakup excitation function at backward angles from α-spectra in the 6Li+144Sm system. Nucl. Phys. A **849**(1), 1–14 (2011). https://doi.org/10.1016/j.nuclphysa.2010.10.001
13. D.H. Luong, M. Dasgupta, D.J. Hinde, R. Rietz, R. Rafiei, C.J. Lin, M. Evers, A. Diaz-Torres, Predominance of transfer in triggering breakup in sub-barrier reactions of ^{6,7}Li with ^{144}Sm, ^{207,208}Pb, and ^{209}Bi. Phys. Rev. C **88**, 034609 (2013). https://doi.org/10.1103/PhysRevC.88.034609

14. S.K. Pandit, A. Shrivastava, K. Mahata, V.V. Parkar, R. Palit, N. Keeley, P.C. Rout, A. Kumar, K. Ramachandran, S. Bhattacharyya, V. Nanal, C.S. Palshetkar, T.N. Nag, S. Gupta, S. Biswas, S. Saha, J. Sethi, P. Singh, A. Chatterjee, S. Kailas, Investigation of large alpha production in reactions involving weakly bound 7Li. Phys. Rev. C **96**(1), 044616 (2017). https://doi.org/10.1103/PhysRevC.96.044616
15. J.P. Fernández-García, M.A.G. Alvarez, L.C. Chamon, Investigation of Coulomb dipole polarization effects on reactions involving exotic nuclei. Phys. Rev. C **92**, 014604 (2015). https://doi.org/10.1103/PhysRevC.92.014604
16. M.A.G. Alvarez, J.P. Fernández-García, J.L. León-García, M. Rodríguez-Gallardo, L.R. Gasques, L.C. Chamon, V.A.B. Zagatto, A. Lépine-Szily, J.R.B. Oliveira, V. Scarduelli, B.V. Carlson, J. Casal, A. Arazi, D.A. Torres, F. Ramirez, Systematic study of optical potential strengths in reactions on ^{120}Sn involving strongly bound, weakly bound, and exotic nuclei. Phys. Rev. C **100**, 064602 (2019). https://doi.org/10.1103/PhysRevC.100.064602
17. M.A.G. Alvarez, M. Rodríguez-Gallardo, J.P. Fernández-García, J. Casal, J.A. Lay, Systematic calculations of reactions with exotic and stable nuclei to establish a unified theoretical approach. Phys. Rev. C **103**, 054614 (2021). https://doi.org/10.1103/PhysRevC.103.054614
18. J. Schwenzel, K. Glasner, P. Niermann, E. Kuhlmann, Isospin mixing observed in the reaction 12C(6Li, a)14N. Nucl. Phys. A **367**(1), 145–156 (1981). https://doi.org/10.1016/0375-9474(81)90282-7
19. W.R. Leo, *Techniques for Nuclear and Particle Physics Experiments: A How-to Approach*, 2nd edn. (Springer, US, 1994). https://doi.org/10.1007/978-3-642-57920-2 . https://cds.cern.ch/record/302344
20. G.F. Knoll, *Radiation Detection and Measurement*, 4th edn. (Wiley, Michigan, 2010)
21. CAEN: 2730 Digitizer Family x2730 - 14 bit 500 MS/s 32 Channels. https://www.caen.it/subfamilies/2730-digitizer-family/. Accessed 02 June 2024
22. CAEN: V2740: 64 Channel 16 bit 125 MS/s Digitizer. https://www.caen.it/products/v2740/. Accessed 02 June 2024
23. CAEN: VX2751: 16 Channel 14 bit 1 GS/s Digitizer with programmable Input Gain. https://www.caen.it/products/vx2751/. Accessed 02 June 2024
24. Mesytec: MDPP-16: 16 channels fast high resolution time and amplitude digitizer. https://mesytec.com/products/nuclear-physics/MDPP-16.html. Accessed 02 June 2024
25. Mesytec: MDPP-32: 32 channels fast high resolution time and amplitude digitizer. https://mesytec.com/products/nuclear-physics/MDPP-32.html Accessed 02 June 2024
26. T. Alharbi, Simple algorithms for digital pulse-shape discrimination with liquid scintillation detectors. Radiat. Phys. Chem. **106**, 50–55 (2015). https://doi.org/10.1016/j.radphyschem.2014.06.031
27. M. Safari, F. Abbasi-Davani, H. Afarideh, S. Jamili, E. Bayat, Discrete fourier transform method for discrimination of digital scintillation pulses in mixed neutron-gamma fields. IEEE Trans. Nucl. Sci. **63**, 325–332 (2016). https://doi.org/10.1109/TNS.2016.2514400
28. Y. Lotfi, S.A. Moussavi-Zarandi, N. Ghal-Eh, E. Bayat, A comparison on three neutron-gamma discrimination methods used with NE213, UGLLT and UGAB scintillators. Radiat. Phys. Chem. **171**, 108701 (2020). https://doi.org/10.1016/j.radphyschem.2020.108701
29. L. Liu, H. Shao, Study on neutron-gamma discrimination method based on the KPCA-GMM-ANN. Radiat. Phys. Chem. **203**, 110602 (2023). https://doi.org/10.1016/j.radphyschem.2022.110602
30. J. Gómez-Camacho, J. García López, C. Guerrero, J.M. López Gutiérrez, R. García-Tenorio, F.J. Santos-Arévalo, E. Chamizo, F.J. Ferrer, M.C. Jiménez-Ramos, M. Balcerzyk, B. Fernández, Research facilities and highlights at the Centro Nacional de Aceleradores (CNA). Eur. Phys. J. Plus **136**, 273 (2021). https://doi.org/10.1140/epjp/s13360-021-01253-x
31. ORTEC: Si Charged Particle Radiation Detectors for Research Applications: B Series Totally Depleted Silicon Surface Barrier Radiation Detector. https://www.ortec-online.com/-/media/ametekortec/brochures/b/b-series-a4.pdf?la=en&revision=189c7eda-d48e-4649-aa61-b76d9eb5d2f3. Accessed 02 June 2024
32. ORTEC: Si Charged Particle Radiation Detectors for Research Applications: D Series Planar Totally Depleted Silicon Surface Barrier Radiation Detector. https://www.ortec-online.com/-/media/ametekortec/brochures/d/d-series-a4.pdf?la=en&revision=59d13606-e7d3-43fb-9b37-50230c57e1f4. Accessed 02 June 2024
33. C. Sheehan, W.J. Lennard, J.B.A. Mitchell, Measurement of the efficiency of a silicon surface barrier detector for medium energy ions using a rutherford backscattering experiment. Meas. Sci. Technol. **11**(8), 5 (2000). https://doi.org/10.1088/0957-0233/11/8/101
34. J.F. Ziegler, M.D. Ziegler, J.P. Biersack, SRIM - The stopping and range of ions in matter (2010). Nucl. Instrum. Methods B **268**(11), 1818–1823 (2010). https://doi.org/10.1016/j.nimb.2010.02.091
35. CAEN: A1422: Low Noise Fast Rise Time Charge Sensitive Preamplifiers. https://www.caen.it/products/a1422/. Accessed 02 June 2024
36. CAEN: DT5423: Quad Linear Desktop Power distributor for A1422 Preamplifiers. https://www.caen.it/products/dt5423/. Accessed 02 June 2024
37. CAEN: V6519: 6 Channel 500 V/3 mA VME HV Power Supply Module. https://www.caen.it/products/v6519/. Accessed 02 June 2024
38. CAEN: 725S Digitizer family: 16/8 Ch. 14-bit 250 MS/s Digitizer. https://www.caen.it/subfamilies/725-digitizer-family/. Accessed 02 June 2024
39. CAEN: V3718: VME to USB 2.0 / Optical Link Bridge. https://www.caen.it/products/v3718/. Accessed 02 June 2024
40. CAEN: VME8008B: 4U 8 Slot VME64 Mini Crate. https://www.caen.it/products/vme8008b/. Accessed 02 June 2024
41. CAEN: Multiparametric DAQ Software for Physics Applications: CAEN Multi-PArameter Spectroscopy Software (CoMPASS). https://www.caen.it/products/compass/. Accessed: 02-06-2024
42. ORTEC: Model 419 Precision Pulse Generator Operating and Service Manual. https://www.ortec-online.com/products/electronic-instruments/pulse-generator/419. Accessed 02 June 2024. https://www.ortec-online.com/-/media/ametekortec/manuals/4/419-mnl.pdf?la=en&revision=4f3afe27-e57c-4813-af11-802e37750430
43. CAEN: DT4800: Micro Digital Detector Emulator. https://www.caen.it/products/dt4800/. Accessed 02 June 2024
44. M. Mayer, SIMNRA, a simulation program for the analysis of NRA, RBS and ERDA. AIP Conf. Proc. **475**(1), 541–544 (1999). https://doi.org/10.1063/1.59188
45. B. Paes, T. Giudice, J. Gómez, D. Abriola, A. Arazi, M.A. Cardona, R.M.I. Betan, D. Hojman, E. Barbará, G. Martí, H. Soler, F. Torabi, B.V. Carlson, J. Lubian, Comprehensive study of the $d + ^{197}$ Au system at near-barrier energies. Phys. Rev. C **110**, 054606 (2024). https://doi.org/10.1103/PhysRevC.110.054606